Ion Temperature Measurements in SSPX

David Auerbach
dauerba1@swarthmore.edu

Swarthmore College Department of Physics
500 College Avenue, Swarthmore, PA 19081

Contents

List of Figures

List of Tables

Ion Temperature Measurements in SSPX

David Auerbach

dauerba1@swarthmore.edu

Swarthmore College Department of Physics

500 College Avenue, Swarthmore, PA 19081

March 21, 2001

Abstract

Using the Ion Doppler Spectrometer (IDS) to measure ion temperatures in the Sustained Spheromak Physics Experiment (SSPX) is described. Background material is presented about plasma physics and about spheromaks, along with a review of optics and spectroscopy. The Doppler broadening of emission lines is derived. The SSPX experiment is described in detail, as is the design and layout of the IDS. Initial ion temperature measurements of around 180 eV are obtained.

1 Introduction

Plasma, by the most accurate definition, is a collection of interacting charged particles in which the coulomb (electrostatic) force plays a significant role in long range interaction. Of course, this is a very broad definition, and encompasses a large number of very different substances. The simplest form is just a gas which has been heated enough such that a large percentage of the molecules in the gas have become ionized, so that the plasma is comprised of positively charged nuclei and negatively charged electrons. These can range in temperature from a few eV (1 eV = 11,604 K) on up. Plasmas comprise a large fraction of the mass in the universe, as most or all of the matter in stars is ionized gasses. They are not, however, very common on earth, because temperatures are so low, and typically to be studied they have to be created artificially in a laboratory. Understanding the behavior of plasmas could have important effects on our lives, because it will allow us a better understanding of many objects in the universe, such as the sun, the earth's magnetosphere, and interstellar plasmas.

There is other potential information obtainable from the study of plasmas. For one thing, because they are ionized, they are good conductors, and can be used to study current flow and magnetic fields, a subject well understood in theory but with complexities that still require further study. One particular aspect of magnetic field behavior that current plasma physics research is directed towards is magnetic reconnection, where magnetic field lines break and connect to other field lines, a phenomenon which is still poorly understood. In addition, one of the major areas of plasma physics research today is an attempt to use laboratory generated plasmas to generate power by heating them enough that nuclear fusion occurs.

There are a multitude of ways to generate, study, and contain plasmas in a laboratory. One of the major issues for all of these methods is containment of plasma. Since the plasma needs to be kept at high temperatures, it needs to be isolated from the lab environment, or the temperature will quickly drop and the ionized gasses will recombine and become atomic gasses again.

One of the most common containment schemes, at least in fusion related plasma physics, is the tokamak, which has been studied in depth for over 30 years. However, recently the feasibility of tokamaks for fusion purposes has begun to be questioned, and other avenues of plasma based fusion energy research, known collectively as magnetic fusion energy (MFE) because the plasmas are magnetically confined, have begun to be pursued. The research that this thesis is based around was conducted on one such experiment, the Sustained Spheromak Physics Experiment (SSPX). A spheromak is a specific laboratory plasma configuration which has the feature that much of the containment of the plasma is due to magnetic fields generated within the plasma itself, rather than by external magnets. This allows the laboratory hardware to be significantly cheaper and simpler than needed for a tokamak, which makes it much more appealing as a potential fusion reactor. While the spheromak has not yet been used to generate plasmas of nearly high enough temperatures for fusion to occur (between 5 and 10 keV), experiments on the CTX experiment at Los Alamos have achieved temperatures of 400 eV, equivalent to temperatures in the initial tokamak experiments that paved the way to the current fusion temperature tokamak reactors today [Hooper, 1996].

This thesis is based around the development of a diagnostic instrument known as an Ion Doppler Spectrometer (IDS), used to measure the ion temperature of hot plasmas (ion temperature is defined in section 2.4). I designed, constructed, and used the instrument over the course of a summer internship and a winter break at the Lawrence Livermore National Lab, where the SSPX is located. In the following sections, I document the process of creating and using the IDS instrument. First, I describe the background physics necessary to understand spheromaks. Then, I describe some of the basics of the related fields of optics and spectroscopy that I used in the creating of the IDS instrument. Then there is a description of the SSPX machine, and an overview of its functionality. Finally, I describe in detail the IDS instrument, describe the process I went through to design and build it, and show some initial ion temperature measurements.

2 The Basics of Plasma Physics

2.1 Magnetohydrodynamics

Plasma, having properties both of a fluid and of a conductor, can be difficult to work with theoretically, because of the large number of particles involves. It typically involves aspects of statistical mechanics, fluid mechanics, and electrodynamics. In addition, in real plasmas there is significant turbulence which is difficult to work with at all, even computationally. However, a fairly simple formulation of plasma behavior does exist, although actually using it to predict plasma behavior exactly can be difficult. The magnetohydrodynamic (MHD) equation of motion, basically $f = ma$ in a more useful form, is written

$$\rho \frac{d\mathbf{U}}{dt} = \mathbf{J} \times \mathbf{B} - \nabla \cdot \mathbf{P} \tag{1}$$

where ρ is the mass density, $\mathbf{U}$ is the velocity vector, and $\mathbf{P}$ is the pressure tensor. This expression can be manipulated into a form which can show how the magnetic force $\mathbf{J} \times \mathbf{B}$ acts. Careful use of vector identities (from [Bellan, 2000]) shows us that

$$\mathbf{J} \times \mathbf{B} = -\frac{1}{2\mu_0} \nabla \cdot \left\{ \begin{bmatrix} B^2 & 0 & 0 \\ 0 & B^2 & 0 \\ 0 & 0 & 0 \end{bmatrix} \mathbf{I}_\perp + \begin{bmatrix} 0 & 0 & 0 \\ 0 & 0 & 0 \\ 0 & 0 & B^2 \end{bmatrix} \hat{B}\hat{B} \right\} \tag{2}$$

where $\mathbf{I}_\perp = \mathbf{I} - \hat{B}\hat{B}$ is a unit tensor perpendicular to the magnetic field. If $\mathbf{P} = P_\perp \mathbf{I}_\perp + P_\parallel \hat{B}\hat{B}$, then the full equation of motion can be written as

$$\rho \frac{d\mathbf{U}}{dt} = -\nabla \cdot \left\{ \begin{bmatrix} P_\perp + \frac{B^2}{2\mu_0} & 0 & 0 \\ 0 & P_\perp + \frac{B^2}{2\mu_0} & 0 \\ 0 & 0 & 0 \end{bmatrix} \mathbf{I}_\perp + \begin{bmatrix} 0 & 0 & 0 \\ 0 & 0 & 0 \\ 0 & 0 & P_\parallel - \frac{B^2}{2\mu_0} \end{bmatrix} \hat{B}\hat{B} \right\} \tag{3}$$

From this, we can see that the magnetic force acts like a pressure perpendicular to the magnetic field, because it adds to the thermal pressure, and that parallel to the magnetic field it acts as a tension opposing the pressure[Bellan, 2000]. This breakdown of the magnetic force is basically the distinction seen between the hoop force, the tendency for a loop of current to expand due to the magnetic field, and the pinch force, which tends to keep bundles of current filaments together. Neither of these statements is strictly correct, because of course the magnetic field does no work, but equation 3 is still valid, as long as the generalization of magnetic fields directly causing motion is avoided.

The relative importance of the magnetic field and the pressure term is typically characterized by the parameter β, defined as

$$\beta = \frac{2\mu_0 P}{B^2} \tag{4}$$

If β is small, than the plasma behavior is dominated by magnetic forces, but if β is large, than hydrodynamic forces dominate the behavior. Spheromaks typically have a low beta, between 0.01 and 0.2 [Bellan, 2000].

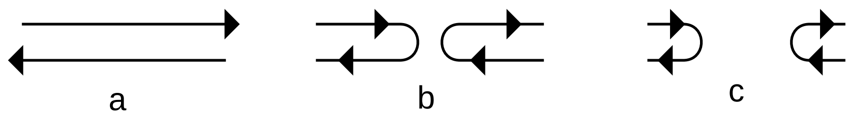

Figure 1: The process of magnetic reconnection. a) A high energy state with two opposing magnetic fields close to each other. b) The magnetic fields break and reconnect in a formation which allows the energy to be reduced. c) Energy in the system decreases as the magnetic fields pull away from each other.

2.2 Flux Conservers

In a perfect conductor, one of the consequences of the high conductance is that the magnetic flux through the conductor cannot change. This is easy to understand, because by definition the change in flux through any surface must be proportional to the electric field around the boundary of that surface. However, the definition of a perfect conductor is that there are no internal electric fields, so there can be no change in flux. This is sometimes described as the flux being frozen into the conductor. Even with a very good conductor, like copper, the rate of change of flux through the metal is slow because of the work required to generate the strong eddy currents needed to change flux.

This condition of 'frozen-in' flux applies to plasmas, as well. Because of the large number of free electrons present in a plasma, it is a very good conductor, and so the lines of magnetic flux are basically attached to the section of plasma they pass through. Thus, if there is a tendency for the magnetic fields to change, the change takes the plasma with it, and vice-versa, if the plasma moves, it tends to drag magnetic field lines with it. This is an important part of the process of generating spheromaks, and also plays a role in the containment of a spheromak once it it generated.

2.3 Magnetic Reconnection

Magnetic reconnection in plasmas is a process that is still not totally understood. Basically, it is when the condition of 'frozen-in flux' from section 2.2 breaks down. When it occurs, the magnetic fields within a conducting plasma change without plasma movement. This typically occurs when the magnetic field configuration is in a high energy state, with opposing magnetic fields pressed up against each other. If the conditions are correct (a situation not that well understood), the magnetic fields can break and join up to the other field, allowing the system to reduce its energy. The process is shown in figure 1. This is one of the major processes that play a role in spheromak formation.

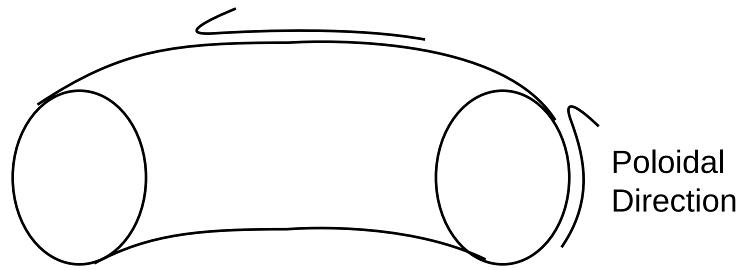

Figure 2: A diagram of the coordinate directions in the toroidal coordinate system.

2.4 Anomalous Ion Heating

Anomalous ion heating is a process related to magnetic reconnection. Like magnetic reconnection, it also is a poorly understood process. An intuitive understanding of it is possible, but there are more complexities to it than are obvious from this explanation. The basic idea is that when magnetic reconnection occurs, there is movement of the magnetic field lines. Because of the 'frozen-in flux' condition, this moves the plasma along with the field lines, resulting in acceleration of the plasma. This acceleration results in preferential ion heating, as more energy goes into the more massive ions than into the electrons ([Ono et al., 1996], [Bellan, 2000]).

Because of this distinction between heating ions and heating electrons, I need to introduce here the concept of ion and electron temperatures (represented as T_i and T_e, respectively). For a specific type of gas, the measure of temperature is proportional to the average kinetic energy of one molecule in the gas. Therefore, if there are two types of particles in a gas (such as ions and electrons in a hot plasma), and each type of particle has a different average kinetic energy, than each species has a distinct measure of temperature. It is the ion temperature T_i that the IDS instrument measures.

2.5 Coordinate Systems for Toroidal Plasmas

Before any further issues are discussed, a definition of the coordinate system typically used for toroidal plasma is important. Figure 2 shows the two principal directions used, poloidal and toroidal. Poloidal is the direction parallel to the surface of a torus which points the short way around the torus, while toroidal is the direction that points the long way around the torus. Thus, when reference is made to toroidal flux, this refers to flux which follows along the torus, while poloidal flux is the kind that loops from the inside to the outside faces of the torus.

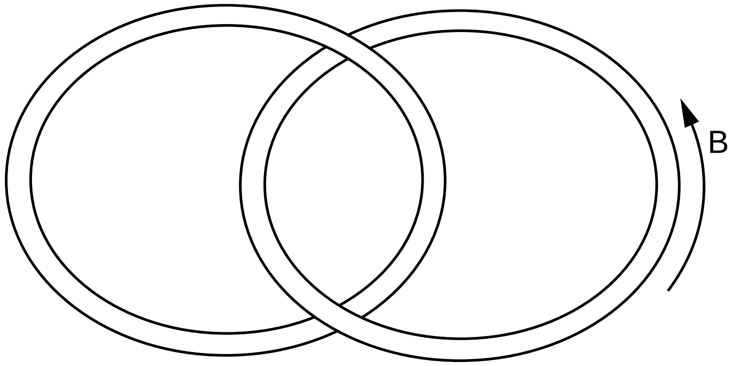

Figure 3: Diagram of linked flux tubes.

2.6 Magnetic Helicity

Magnetic helicity, very generally, is a measure of how twisted magnetic field lines are. This can be either loops of magnetic flux linking with each other (figure 3), or a single tube of flux twisted as it loops (like a Möbius strip, for example), or a tube of flux crossing over itself. These three concepts all reduce to the same situation, as you can cut a tube with a full twist in it in in half and end up with two linked flux tubes, and if you straighten out a flux tube crossing itself you get a flux tube with a twist in it. It is a very important concept for spheromak physics, as the amount of helicity contained in a spheromak affects important factors such as confinement and decay (see section 3).

Magnetic helicity is is defined as

$$K = \int_V \mathbf{A} \cdot \mathbf{B} d^3 r \tag{5}$$

where $\mathbf{A}$ is the magnetic vector potential, and $\mathbf{B}$ is the magnetic field. A physical interpretation of equation 5 is obtainable by considering several cases, it becomes more clear. The first case is the one of linked flux tubes (figure 3). Since $\mathbf{B}$ vanishes outside of the two tubes, we can break the integral up into the two volumes and consider them separately. Thus, for the first tube, we just have the integral in equation 5 over the volume of the first tube. We can then rewrite equation 5 for the volume of the first flux tube as

$$K_1 = \oint_{c_1} \int_{S_1} (\mathbf{A} \cdot d\mathbf{l})(\mathbf{B} \cdot d\mathbf{s}) \tag{6}$$

[Bellan, 2000] where the path C_1 is around the flux tube, the surface S_1 is a cross section of the flux tube, and K_1 is the helicity of the first tube. It is not immediately obvious why this can be done, but the result is that each differential length element is paired with the portion of the integrand that will contribute along it. Thus, the surface integral in equation 6 is just the flux of the tube Φ_1, and is a constant of integration, so it can be brought outside the path integral. Then, since $\nabla \times \mathbf{A} = \mathbf{B}$, we can apply Stokes theorem to find that the remaining integral is simply the flux Φ_2 of the second tube, as that is the only magnetic flux through the integration path. Thus, the helicity K_1 is just $\Phi_1\Phi_2$, the product of the flux of each tube. A similar argument shows that K_2 is exactly equal to K_1, so the total helicity of the system, because we just add the two integrals, is

$$K = 2\Phi_1\Phi_2 \tag{7}$$

The second case, that of a single flux tube twisted on itself, is a more difficult derivation, and I won't go through it here, and instead will just cite the result from [Bellan, 2000]. However, the result does make sense intuitively given equation 7, because of the topological relationship to the previous case. The helicity of a twisted flux tube of flux Φ is

$$K = T\Phi^2 \tag{8}$$

where $T = d\psi/d\phi$ is just the number of full twists in the tube. Thus, a tube of flux Φ with one whole twist would have a helicity of Φ^2, whereas a flux tube with half a twist (as in a Möbius strip) would have a helicity of $\frac{1}{2}\Phi^2$. In equation 8, T is the inverse of the safety factor for toroidal plasmas, which is the number of times the flux goes in a full loop toroidally for one poloidal 'twist'.

Magnetic helicity is an important concept for spheromak physics because the quantity of helicity in a spheromak has been experimentally shown to be a conserved quantity with regard to small scale turbulence, which is where much of the magnetic energy of a spheromak is dissipated. A fairly intuitive explanation of this phenomenon is possible, however. For any specific region of space, magnetic energy and helicity scale differently. Specifically, since magnetic energy W is found by

$$W = \int \mathbf{B}^2 d^3r \tag{9}$$

it is obviously of scale B^2L^3, where L is a linear dimension. Helicity, as mentioned before is found by

$$K = \int \mathbf{A} \cdot \mathbf{B} d^3r \tag{10}$$

Since $\mathbf{B} = \nabla \times \mathbf{A}$, $\mathbf{B}$ must be proportional to $\mathbf{A}L$, so helicity must scale like B^2L^4. Thus, as length scales get smaller, the proportionality of magnetic energy to helicity scales like L^{-1}. Thus if there is a dissipative process that happens on a small length scale, such as magnetic reconnection or turbulence (two related processes), the magnetic energy lost is much larger than the helicity lost. Thus, at least on short time scales, magnetic energy is lost while helicity is conserved.

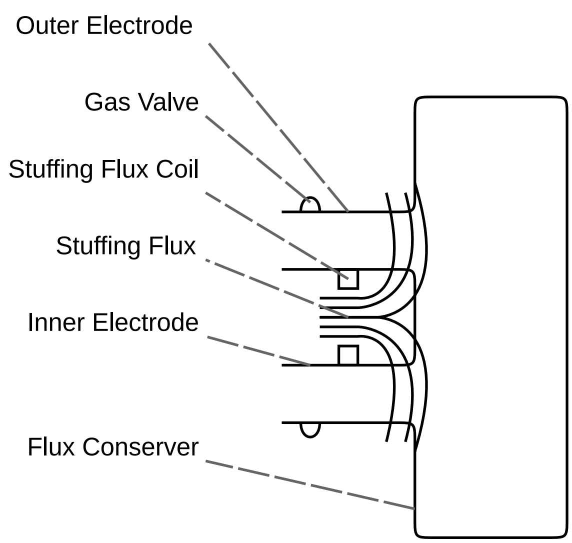

Figure 4: The Basic Layout of a coaxial gun for spheromak formation

3 Spheromaks

We now have the tools needed to talk about how to generate spheromaks. In this discussion, I will only cover one particular method for generating these structures; in fact there are several proven laboratory techniques for creating spheromaks. The method I will describe is known as coaxial injection, and it is the method used in SSPX. I will first describe the actual formation techniques, then I will talk about the theory behind spheromak formation. Finally, I will discuss techniques for sustaining spheromaks to keep them from cooling off and decaying.

3.1 Coaxial Injection

The basic design for a coaxial gun used for spheromak formation is shown in figure 4. The main components are the inner and outer electrodes, which are connected to the external power supply, the copper flux conserver, the circular electromagnetic coil which puts a magnetic field, known as the stuffing flux, across the mouth of the gun, and the gas valves. The apparatus is cylindrically symmetric, and the diagram is a cross section. The entire apparatus is contained in a vacuum chamber.

The formation process is outlined in figure 5. It begins with the stuffing field coils turning on well before the actual firing, to allow the generated flux to soak into the conducting metal of the inner and outer electrodes (see flux conservers, sec 2.2). At the beginning of the firing of the gun, hydrogen gas is puffed into the area between the electrodes at the gas valves. Then, a high potential is put

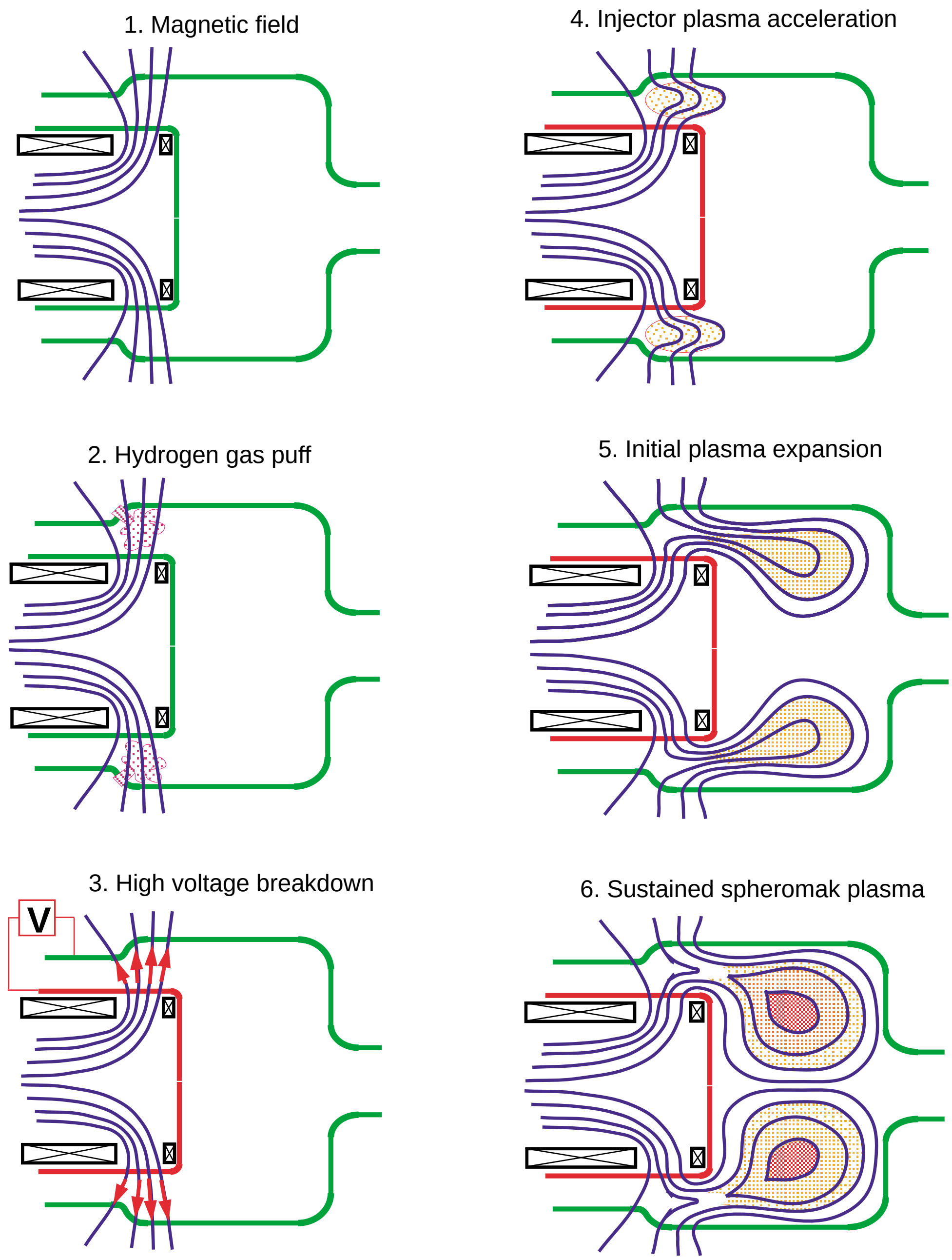

Figure 5: An overview of the formation process of spheromaks by coaxial injection [Hill et al., 2000a]

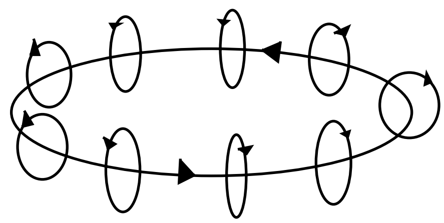

Figure 6: The Magnetic fields of a spheromak, broken down into poloidal and toroidal components

between the electrodes, which causes the hydrogen gas to ionize and conduct current from external capacitor banks. This is shown in parts 1 though 3 of figure 5.

The current flowing in the gun causes a toroidal magnetic field (that is, around the inner electrode) to form in the newly ionized hydrogen plasma. This current flows down the inner electrode, radially outward through the plasma, and then up the outer electrode. Once this B field is in place, there is current and magnetic field in the same location, causing a $J \times B$ force which accelerates the plasma down the barrel of the gun towards the opening of the barrel (figure 5, part 4). The plasma then encounters the flux across the end of the gun, and because of the frozen in flux condition, the stuffing flux is dragged out into the flux conserver and wraps around the outside of the tube of plasma as poloidal flux (part 5). Then reconnection occurs, separating the poloidal flux surfaces of the torus from the stuffing flux. Once this separation occurs, the spheromak expands into its final form, known as a Taylor state [Taylor, 1974] (see section 3.2). Because of the inability for magnetic flux to move quickly through the copper of the flux conserver, it acts as a stabilizer, keeping the spheromak from shifting from side to side or rotating out of its original plane.

As we can see from the fact that the configuration involves linked poloidal and toroidal flux, the spheromak is generated with a certain amount of helicity, which is conserved, at least on the time scale of the formation process. In fact, it is the gradual resistive and turbulent decay of the helicity that eventually causes the spheromak to decay. Although it typically makes more sense to think about the magnetic field lines as having a helical structure, we can imagine the poloidal and toroidal flux in the spheromak as having the formation shown in figure 6. By comparing this to figure 3, in section 2.6, we can see that the total helicity of a spheromak is just

$$K_{spheromak} = 2\Phi_{pol}\Phi_{tor} \tag{11}$$

where Φ_{pol} is the total poloidal flux in the spheromak, and Φ_{tor} is the toroidal flux.

3.2 Taylor States

The theoretical configuration of a spheromak, with its currents and magnetic fields, can be theoretically derived, and in fact it can be proved that this configuration has the minimum possible energy given the initial amount of helicity. There are two distinct ways to derive this result, one of which is more intuitively obvious, and the other more mathematically rigorous. Both derivations will be presented here.

The first begins with the basic MHD equation of motion,

$$\rho \frac{d\mathbf{U}}{dt} = \mathbf{J} \times \mathbf{B} - \nabla \cdot \mathbf{P} \tag{12}$$

We first assume that there is a relaxed configuration, with all forces balanced (known as a 'force free' configuration) to which the plasma can relax. From this assumption, we can see that both sides of equation 12 will be zero. Then, since we know experimentally that spheromaks have low β, we know that the second term on the right hand side of equation 12 is negligible compared to the first term. This gives us the fact that, in the relaxed state,

$$\mathbf{J} \times \mathbf{B} = 0 \tag{13}$$

From this, we can see that all currents must be flowing parallel to the magnetic fields. Since Maxwell's equations tell us that $\nabla \times \mathbf{B} = \mu_0 \mathbf{J}$, we can write down

$$\nabla \times \mathbf{B} = \lambda \mathbf{B}, \tag{14}$$

a differential equation which defines the magnetic field. This is basically an eigenvalue problem, and the solutions, which will be shown in a moment, do indeed describe the configuration of a spheromak very well.

First, however, I will show that by assuming that a spheromak is a configuration of minimum magnetic field for a given amount of helicity, the spheromak configuration can be derived. This derivation also assumes that the spheromak is isolated, with a perfectly conducting bounding surface that has no magnetic flux through it. This is not generally the case in a real world experiment, but the actual results without assuming isolation are similar. From the isolation condition, we know that on the boundary surface,

$$\oint_c \mathbf{A} \cdot dl = 0 \tag{15}$$

Since the there can be no electric field on the bounding surface, we can draw the conclusion that there is no change to the components of the vector potential tangential to the bounding surface, of in differential calculus notation, $\delta \mathbf{A}_{\parallel} = 0$.

We can now write down the variational equation

$$\delta W - \lambda \delta K = 0 \tag{16}$$

in which we are minimizing magnetic energy $W = \int B^2/2\mu_0 d^3r$ subject to $K = \int \mathbf{A}\cdot\mathbf{B}d^3r$ being a constant. This can be re-written as

$$\int \mathbf{B}\cdot\delta\mathbf{B}d^3r - \lambda\int(\mathbf{A}\cdot\delta\mathbf{B}+\mathbf{B}\cdot\delta\mathbf{A})d^3r = 0 \tag{17}$$

where λ is absorbing all the constants in the equation. We use the fact that $\delta\mathbf{B} = \nabla\times\delta\mathbf{A}$ to rewrite equation 17 as

$$\int \mathbf{B}\cdot\nabla\times\delta\mathbf{A}d^3r - \lambda\int(\mathbf{A}\cdot\nabla\times\delta\mathbf{A}+\mathbf{B}\cdot\delta\mathbf{A})d^3r = 0 \tag{18}$$

We can then apply the vector identity

$$\nabla\cdot(\mathbf{Q}\times\mathbf{R}) = \mathbf{R}\cdot\nabla\times\mathbf{Q} - \mathbf{Q}\cdot\nabla\times\mathbf{R} \tag{19}$$

and replace both terms involving a curl in equation 18 to get

$$\int(\delta\mathbf{A}\cdot(\nabla\times\mathbf{B}) + \nabla\cdot(\delta\mathbf{A}\times\mathbf{B}) - \lambda\nabla\cdot(\delta\mathbf{A}\times\mathbf{A}) - 2\lambda\mathbf{B}\cdot\delta\mathbf{A})d^3r = 0 \tag{20}$$

The two terms in equation 20 involving the divergence can be transformed into surface integrals using Gauss's law. However, both of them go to zero, because of the isolation condition $\delta\mathbf{A}_\parallel = 0$. Combining the two remaining terms gives

$$\int \delta\mathbf{A}\cdot(\nabla\times\mathbf{B} - \lambda\mathbf{B})d^3r = 0 \tag{21}$$

Now, since we know that $\delta\mathbf{A}$ is arbitrary due to gauge choice, we have

$$\nabla\times\mathbf{B} = \lambda\mathbf{B} \tag{22}$$

which is exactly the same differential equation given in equation 14.

The solutions to this differential equation, solved in cylindrical coordinates, are as follows, where $\bar{B}$ is a variable for the strength of the magnetic fields, k and m are simply order numbers for the solution, and $\gamma = \sqrt{\lambda^2 - k^2}$:

$$\begin{aligned}
B_r(r,\phi,z) &= -\frac{\bar{B}}{\gamma}\left(\frac{m\lambda}{\gamma r}J_m(\gamma r) + kJ'_m(\gamma r)\right)\sin(m\phi + kz) \\
B_\phi(r,\phi,z) &= -\frac{\bar{B}}{\gamma}\left(\frac{mk}{\gamma r}J_m(\gamma r) + \lambda J'_m(\gamma r)\right)\cos(m\phi + kz) \\
B_z(r,\phi,z) &= \bar{B}J_m(\gamma r)\cos(m\phi + kz)
\end{aligned} \tag{23}$$

[Bellan, 2000]. These equations describe very well experimental observations of magnetic field configurations in spheromaks.

3.3 Sustainment

The decay of spheromaks is basically due to the decay of the helicity due to resistive dissipation in the plasma. Thus, in order to keep a spheromak from decaying, it is necessary to add helicity to the plasma while it is still in an ordered configuration. This is known as helicity injection.

The way helicity injection works is as follows. The poloidal component of the flux in a spheromak is solely dependent on the magnitude of the preliminary stuffing flux, which, because it is generated before the formation occurs, is of a constant magnitude. Thus, it is the toroidal flux generated in the gun which affects the magnitude of the helicity (naturally, this is something of an oversimplification). We can write the time derivative of helicity as

$$\dot{K} \cong 2\Phi_{pol}\dot{\Phi}_{tor} \tag{24}$$

We know that the time derivative of a flux is an electromotive force, so basically for a certain voltage across the electrodes of the gun,

$$V_{gun} = \dot{\Phi}_{tor} \tag{25}$$

and thus

$$\dot{K} = 2V_{gun}\Phi_{pol} \tag{26}$$

Thus, keeping a voltage across the electrodes of the gun adds helicity even after formation has occurred.

The actual dynamics are more complicated. One basic idea is that the continued voltage across the gun generates a second, smaller spheromak, which is collided into the back of the first, and which then gets absorbed and the helicity gets coupled into the main spheromak. One concern about using this method to drive a spheromak is that, in the process of absorbing helicity, the closed flux surfaces of the main spheromak are broken. Since it is primarily the closed flux surfaces which are responsible for the containment of the hot plasma, this method may not be ideal. Another way this can work is that current will flow from the electrodes along the open flux surfaces surrounding the spheromak, adding more toroidal flux. Part of the purpose of SSPX is to experiment with helicity injection and determine how viable the process is for heating a spheromak [Hooper et al., 1998].

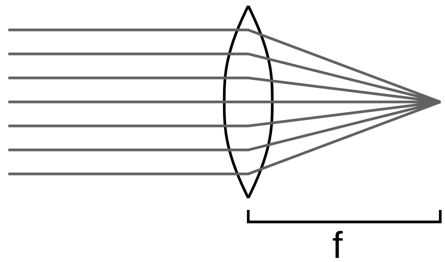

Figure 7: Collimated, or parallel, light rays converge at the focal length f from the lens

4 Optics

Designing the Ion Doppler Spectrometer, which is primarily an optical instrument, required a thorough understanding of the physics of optics in order to achieve functionality. A basic review of the optics used in its design and construction is presented here.

4.1 Thin Lenses

There are two basic equations that can be used in most cases when using thin lenses (where thin means that the thickness of the lens is small compared to the distance between the object and the lens) or mirrors to manipulate light. The first is the thin lens equation,

$$\frac{1}{s} + \frac{1}{s'} = \frac{1}{f}\,, \tag{27}$$

where s is the distance of the object from the lens, s' is the distance of the object's image from the lens, and f is the focal length of the lens. The focal length of a lens is the distance from the lens at which parallel light rays converge (see figure 7). The second principal equation,

$$m = -\frac{s'}{s} \tag{28}$$

defines the magnification of the image. A negative magnification simply means that the image has been inverted.

A third important concept used frequently in the course of designing and building the IDS is the focal ratio, or f-value, of a lens. This is defined by

$$f\ value = \frac{f}{a} \tag{29}$$

where a is the diameter of the lens, and f is again the focal length of the lens. This is frequently written as f/#, that is, if a lens has an f-number of 5, it is described as a f/5 lens.

5 Spectroscopy

The main tool used for this research was spectroscopy. The following sections review some of the basics of spectroscopy and how it is applied to measuring temperatures in plasmas.

5.1 Radiation From Excited Atoms

In plasmas, the high temperatures and resulting high velocity collisions between particles are the main cause of the ionization of the atoms. However, the free electrons are constantly getting captured by the nuclei in the plasma and dropping back into bound states. Thus, there is a continuous process of electrons getting knocked into higher energy states and then dropping back into lower energy states. This is true both between free electron states and bound states, and between higher and lower energy bounds states, as the collisions between atoms can either free the electrons completely from the nuclei, or just knock them into higher energy bound states.

Between any two bound states, there is an exact, quantum mechanically defined difference in energy, and when an electron drops to a lower energy state, the difference in energy is typically given off as a single photon. Thus, for a specific nucleus, there is a certain set of wavelength photons that will be released as electrons move between the energy levels. Thus, there are specific, discrete spectral lines that are emitted from hot plasmas, and it is these lines that are used to get temperature data from the plasma.

5.2 Doppler Shift and Broadening of Spectral lines

In a gas with weak molecular interactions, the particles (all of mass m) have a Maxwellian distribution of velocities. This is defined as

$$f(v,T) = \left(\frac{m}{2\pi kT}\right)^{\frac{3}{2}} e^{-\frac{mv^2}{2kT}} \tag{30}$$

where $f(v,T)$ is the probability that a particle in a gas of temperature T will have a velocity v [Reif, 1965]. We are interested in using the Doppler shift of emitted radiation to measure this velocity distribution (and so measure temperature), so we want to integrate over the velocities perpendicular to the line of sight. This gives us

$$f(v_x,T) = \left(\frac{m}{2\pi kT}\right)^{\frac{1}{2}} e^{-\frac{m{v_x}^2}{2kT}} \tag{31}$$

where x is the line of sight direction. This is a simple gaussian distribution.

Now, if a particle emitting radiation of frequency ν is moving towards a detector at velocity v, the then detected frequency ν_d is given by

$$\nu_d = \nu \left(\frac{1+\frac{v}{c}}{1-\frac{v}{c}}\right)^{\frac{1}{2}} \tag{32}$$

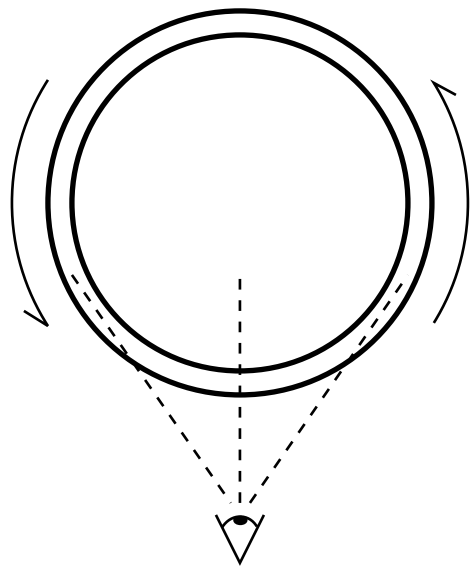

Figure 8: Three views of a spheromak used to determine rotational velocities

For small velocities v equation 32 can be approximated as

$$\nu_d = \nu \left(1 - \frac{v}{c}\right)^{-1} \tag{33}$$

from which we can find

$$\frac{\Delta\nu}{\nu} = \frac{v}{c} \tag{34}$$

Substituting v in equation 34 into equation 31 gives us the distribution of frequencies

$$f(\nu, T) \propto exp\left[-\frac{mc^2\left(\frac{\Delta\nu}{\nu}\right)^2}{2kT}\right] \tag{35}$$

From equation 35, we can find that the half width half maximum of the dispersion (defined as half the spectral width of the gaussian at half the intensity of the maximum) is

$$hwhm = \sqrt{\frac{(2\ ln\ 2)kT}{mc^2}} \tag{36}$$

This dispersion is what is seen in a Doppler broadened spectral line.

The Doppler shift can also be used to measure rotational velocities in a spheromak. Light can be collected along the three views shown in figure 8. If

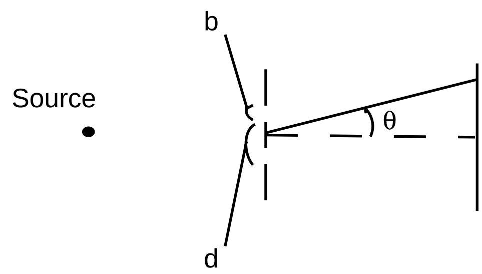

Figure 9: The double slit experiment

the plasma is rotating, the two views along the plasma (as opposed to down the center) will be red and blueshifted. While it is very difficult to pinpoint with enough precision the exact spectral location of a line, the difference between the recorded location of a line along each of the views can give a rotational velocity using equation 33.

5.3 Diffraction

Diffraction gratings work on the principal of constructive and destructive interference of electromagnetic waves, and on the fact that plane electromagnetic waves passing through a narrow slit will be converted into spherical waves originating at the slit, which can constructively or destructively interfere with other spherical waves. The simplest example of these two effects is the double slit experiment.(This derivation follows [Jenkins and White, 1976]). If light from a single source is passed through two slits of width b which are a distance apart d, then projected onto a screen, the intensity of the light on the screen due to the interference between the two waves is

$$I = 4{A_o}^2 \frac{\sin^2\beta}{\beta^2} \cos^2\gamma \tag{37}$$

where

$$\beta = \frac{\pi}{\lambda} d \sin\theta \; ,$$
$$\gamma = \frac{\pi}{\lambda} b \sin\theta \; ,$$

A_0 is the original intensity of the light, and θ is the angle from the slits at which a particular point on the screen is located (see figure 9). In this expression, the $\sin^2$ term is the result of diffraction of the light through the slits, and the $\cos^2$ term is from the interference of the two waves at the screen.

In a situation with N slits, the pattern on the screen is described by

$$I = {A_o}^2 \frac{\sin^2\beta}{\beta^2} \frac{\sin^2 N\gamma}{\sin^2\gamma} \tag{38}$$

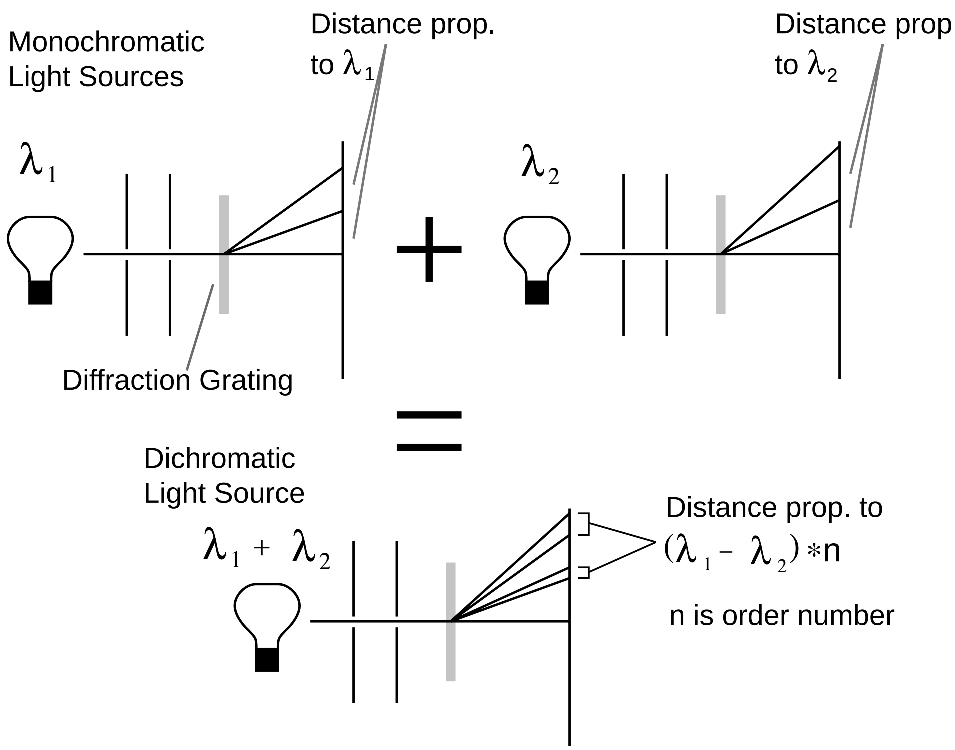

Figure 10: An example of how the spectrum of dichromatic light is formed by a diffraction grating

The maxima of equation 38 are that of the factor involving $\sin\gamma$, because that term's maxima are so large. We can see this by taking the appropriate limits and then applying L'Hopital's rule,

$$\lim_{\gamma\to m\pi}\frac{\sin N\gamma}{\sin\gamma} = \lim_{\gamma\to m\pi}\frac{N\cos\gamma}{\cos\gamma} = \pm N \tag{39}$$

These principal maxima occur when $d\sin\theta$ is equal to an integral multiple of the wavelength λ being passed through the grating. As the number of slits N increases, the brightnesses of the principal maxima increase over the rest of the pattern. In addition, the maxima become more and more narrow as N increases.

The property of diffraction by a large number of slits (known as a diffraction grating) that makes it so useful for spectroscopy is the fact that the locations of the maxima on the screen are proportional to the wavelength of the light being diffracted. As an example (see figure 10), if two different frequencies of light are being passed through the slits at once, their first maximum will of course be at θ equals 0. However, between the first and second maximum there will be a distance proportional to λ, and for the third, fourth, fifth, etc., there will be a distance proportional to 2λ, 3λ, 4λ, etc. This results in the spectrum of the incoming light being displayed on the screen. Not only that, but several duplicates of the spectra are displayed, one per maxima of equation 38. Each of these spectra is known as an order, and each successive order is has a larger dispersion between the wavelengths in the spectrum. The general equation for the location of a spectral line is given by

$$d(\sin i + \sin\theta) = m\lambda\,, \tag{40}$$

where i is the angle of incidence of the light on the slits, θ is the angle at which the line for wavelength λ will be at, and m is the order number (1,2,3, etc.).

5.4 Spectrometers

In a spectrometer, the spectrum of light is examined using the principals of light diffracting through N small slights derived in section 5.3. However, instead of having light pass through a large number of slits, a large number of closely spaced lines are inscribed on a mirrored surface. This is known as a diffraction grating. It is primarily the diffraction grating, along with the focal length of the spectrometer, that define the properties a spectrometer.

A basic spectrometer is shown in figure 11. Light hits a narrow entrance slit that limits the amount of light coming into the spectrometer and causes the generated spectrum to be made up of a series of vertical lines, because the spectrum is made up of a series of projected images of the slit. The incoming light is collimated by a curved mirror, then projected onto a diffraction grating, which in turn reflects the light onto a second curved mirror, which focuses the light onto the output plane, where a camera or other type of detector images the spectrum. There are many different layouts for spectrometers, but all follow this same basic concept.

For high resolution spectroscopy, there are two important aspects of the spectrum created by a spectrometer. The first is the dispersion of the spectrum, which characterizes the separation between two different wavelengths. The angular dispersion, which can be obtained by differentiating equation 40 with respect to λ, is

$$\frac{d\theta}{d\lambda} = \frac{m}{d\cos\theta} \tag{41}$$

To find the linear dispersion, we can simply multiply the angular dispersion in equation 41 by the focal length of the spectrometer, L, and invert the equation to get

$$\frac{d\lambda}{dx} = \frac{d\cos\theta}{mL} \tag{42}$$

In both of the previous expressions, it is useful to realize that the width d of the slits or lines on the grating can be replaced by the inverse of the line density of the grating in lines per unit length, which is how diffraction gratings are usually classified.

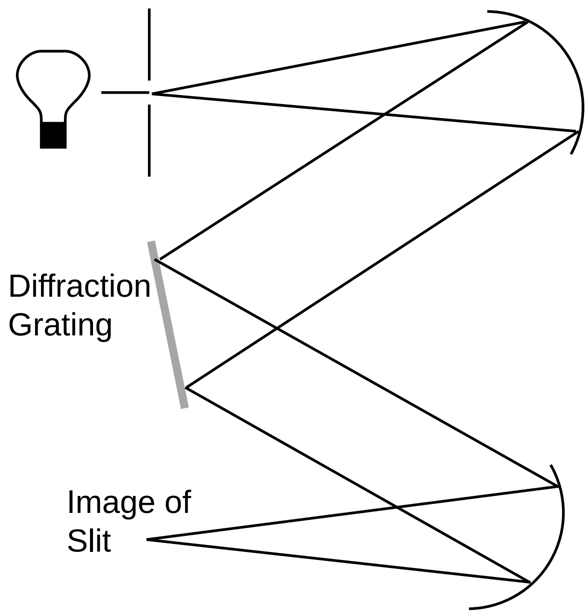

Figure 11: A diagram of a basic spectrometer layout. The mirrors and grating are enclosed in a light tight box.

The second important quality of a high resolution spectrometer is the width of the spectral lines generated. The theoretical minimum difference between the wavelength of two distinguishable spectral lines is defined by the width of the principal maxima of equation 38. It can be shown that this minimum distance, the resolving power of the grating, is

$$\frac{\lambda}{d\lambda} = mN \tag{43}$$

However, there are other causes of line broadening within an instrument (that is, ignoring external effects such as Doppler broadening) that contribute to making the actual line seen at the output of the spectrometer wider than the theoretic minimum. One of the largest contributors to instrumentally caused line broadening is the finite width of the input slit. Because the spectral lines are in fact images of the input slit, the width of the lines can be no smaller than the width of the slit, and in general this is larger than the theoretical minimum. Other widening effects can be caused by aberrations or misalignment in the optics of the spectrometer.

6 SSPX

The SSPX experiment is based at the Lawrence Livermore National Laboratory (LLNL) in Livermore, CA. It was designed and is maintained and run by a team of physicists at the lab, and by a number of outside collaborators who have worked on specific diagnostic equipment for the experiment and on computational models of the device and the plasmas it generates. This section will be an overview of the experiment, its basic functionality, and the diagnostic equipment used to record what is going on during the formation, sustainment, and decay of the spheromak plasmas it generates.

6.1 Layout

The experiment is based around a coaxial gun connected to a 1.2 cm thick copper flux conserver, shown in figure 12. The flux conserver has a diameter of 1 meter, a minor radius for the plasma of 0.23 m, and a diagnostics slit at the height of the toroidal axis of the plasma. The interior surface of the flux conserver is coated with a thin, plasma-sprayed coating of tungsten to help keep contamination levels low. The entire apparatus is contained in a large vacuum chamber, which has diagnostic access ports at the level of the slit in the flux conserver. There is a titanium gettering apparatus that can be inserted into the center of the flux conserver, which sprays a thin layer of titanium onto the interior of the flux conserver. The titanium also helps to keep impurity levels in the plasma low by reacting with particles that encounter the flux conserver and making them stick to the surface. The co-axial gun is attached to two separate capacitor banks. The first is a 0.5 MJ, 10 kV formation bank used to generate the spheromaks. The second is a 1.5 MJ, 5 kV bank used to sustain the spheromak after it is formed. These banks are separately fired by sets of ignitron switches.

There are several sets of magnet coils which produce initial flux inside the flux conserver before a shot is fired. The two coils which generate stuffing flux are located inside of the inner electrode, and produce flux that crosses the opening of the gun radially. More recently, a set of 6 bias field coils were installed. These coils cause the initial magnetic field to be exactly parallel to the surfaces of the flux conserver. These flux surfaces should reduce the amount of contact the hot plasma has with the cold walls. The gas for the plasma is injected at the top of the coaxial gun by a ring of gas valves. These can be connected to either hydrogen gas or helium gas, which is used for helium discharge cleaning.

All of the equipment for the firing process is under computer control. A Macintosh running Labview controls all of the timing and hardware. There is remote control of basically all of the equipment, from power supplies to gas valves to data collection, so that parameters for a shot can be set at one location.

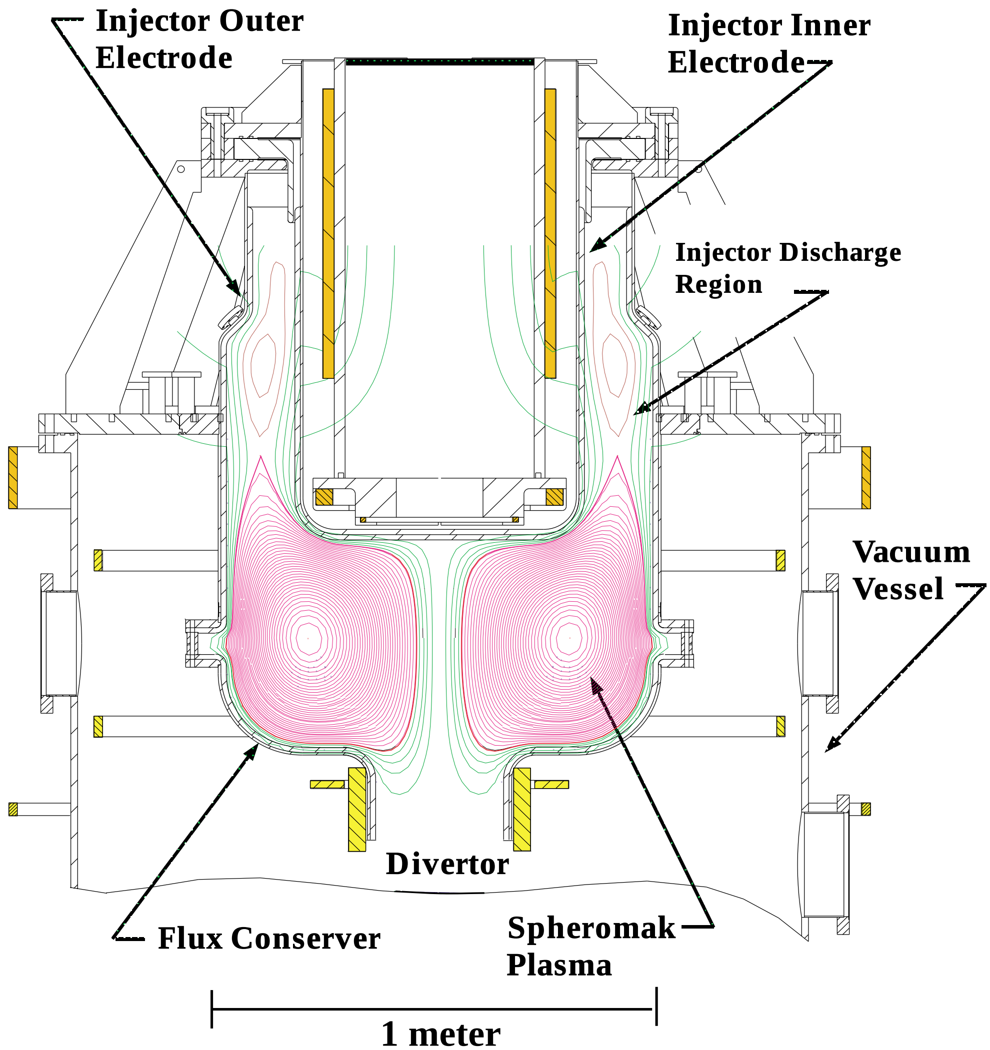

Figure 12: A schematic of the interior of SSPX

6.2 Diagnostic Equipment

There is a huge array of diagnostic instruments to record various data about each plasma shot. The diagnostic equipment comes from a variety of different collaborative institutions as well as from the SSPX team at LLNL. Full details can be found in [McLean et al., 2001], but here briefly are some of the more important diagnostic instruments on the SSPX.

There are Rogowski coils on the power cables to the electrodes, which are used to measure current, and there is a high voltage probe at the electrodes, which together can be used to measure power input ($P = IV$). Along the flux conserver there are magnetic field pickup coils, which provide data that can be used to model the internal magnetic structure of the spheromak. A CO_2 laser interferometer is used to take density measurements, and a spectrometer gives a measure of impurity concentrations in the plasma by the intensities of their emission lines. The IDS spectrometer described in this report provides a measure of the Ion Temperature, and there is a new Thomson scattering system, just coming online, which can provide a profile measurement of electron temperature at 10 points along the radius of the plasma.

6.3 Operations

When operated, the device produces spheromaks with a lifetime of between 1.5 and 2.0 ms. 2 Torr-l of hydrogen gas are injected into the gun region, and approximately 0.25 ms later the formation bank is triggered. Breakdown (the initial flow of current through the hydrogen gas) timing varies, typically occurring about 0.25 ms after the triggering of the formation bank, and approximately 0.25 seconds after the initial breakdown the sustainment bank fires. The efficiency, estimated magnetic energy divided by energy input, is around 15%. Initial electron temperature measurements from the Thomson scattering instrument show electron temperatures around 120 eV along the magnetic axis. Figure 13 shows data collected from a typical SSPX shot.

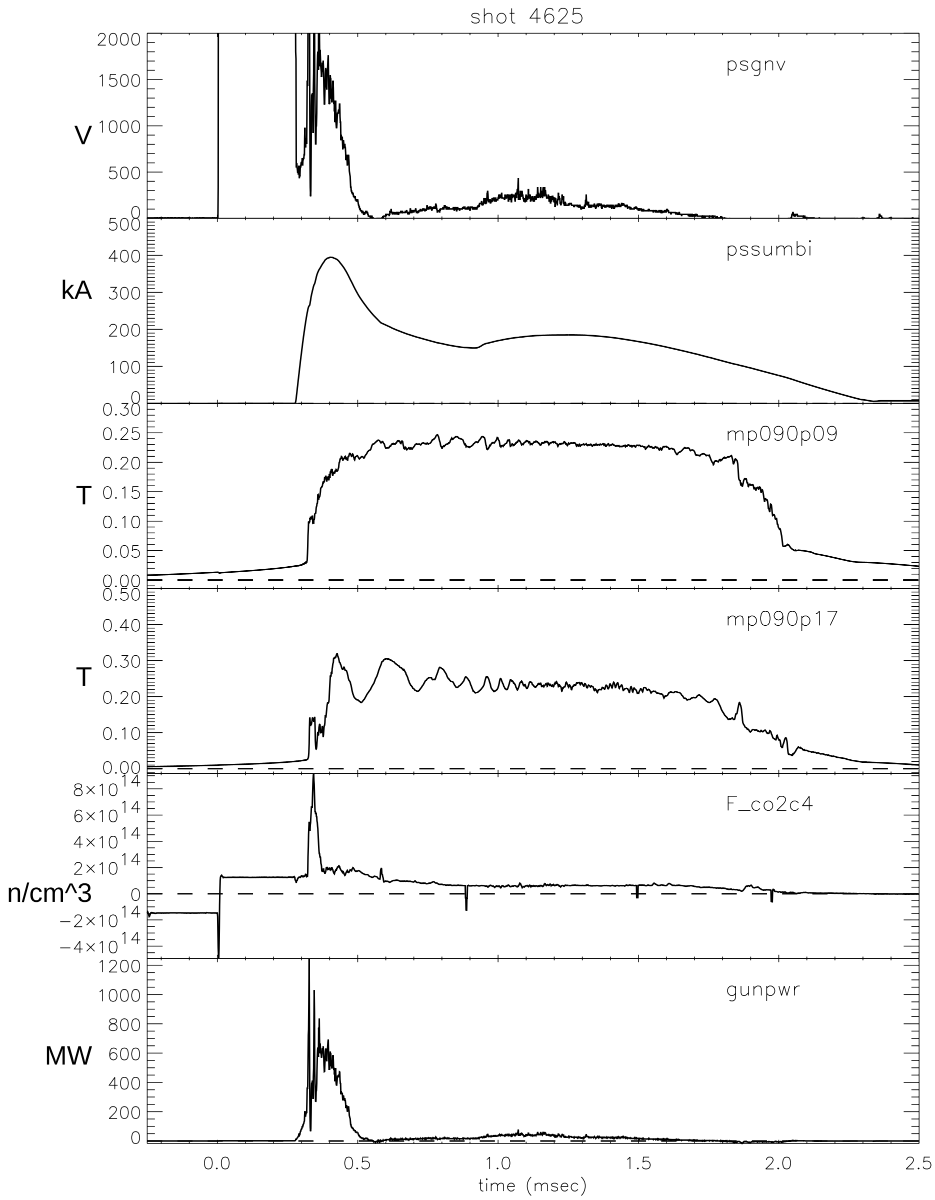

Figure 13: Typical SSPX shot data. The plot psgnv is gun voltage, pssumbi is gun current, the two mp090 plots are data from two different magnetic probes on the flux conserver, F_co2c4 is a density measurement from the co2 interferometer, and gunpwr is total instantaneous gun power.

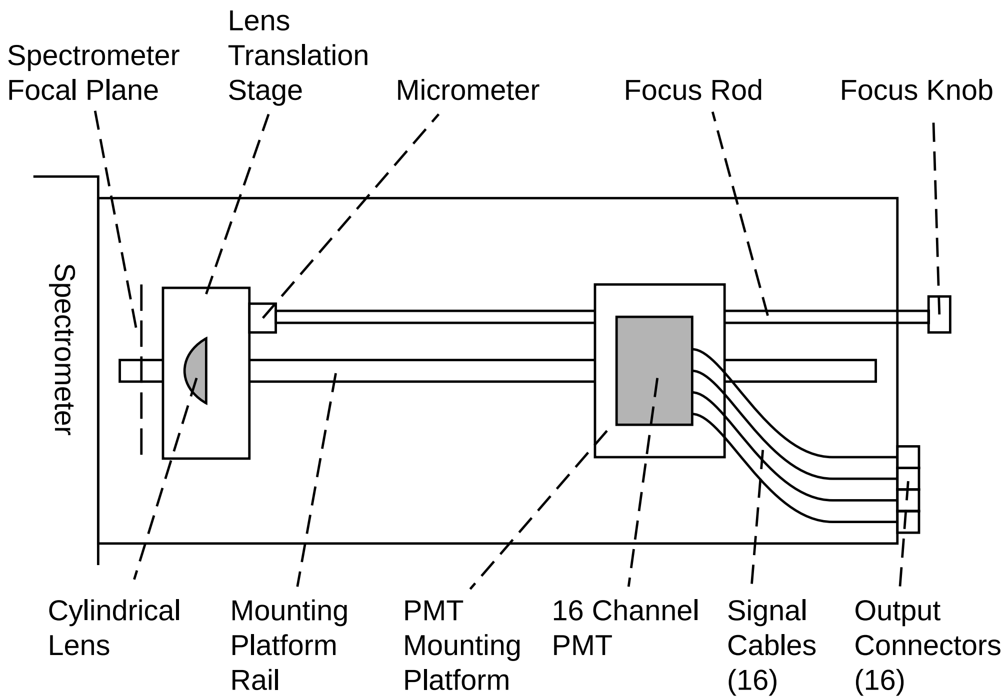

Figure 14: A detailed schematic of the IDS detector assembly

7 IDS-The Ion Doppler Spectrometer

7.1 Layout

The Ion Doppler Spectrometer (IDS) for SSPX is based around a 1 meter focal length high resolution spectrometer. Attached to it is a custom detector assembly. The design and assembly of this detector box was one of the primary focuses of my project. The spectrometer itself is an Instruments S.A. model THR1000 spectrometer, and has a diffraction grating with a line density of 2400 lines/mm, blazed for first order spectra between 300 and 600 nm.

Light is collected for the IDS at a port on the vessel at the level of the diagnostics slit in the flux conserver. Mounted directly outside of the clear window of the port is a telescope with a 5” focal length collection lens, focused so that one end of a fiber optic bundle is exactly at the focal point of the lens. The result of this placement is that the fiber only collects light from a column of plasma the size of the lens. The orientation of the telescope is adjustable, so that the light can be collected along 5 different chords crossing the chamber (figure 16). This allows the temperature at different locations in the spheromak to be measured, and allows the rotational velocity to be measured (see section

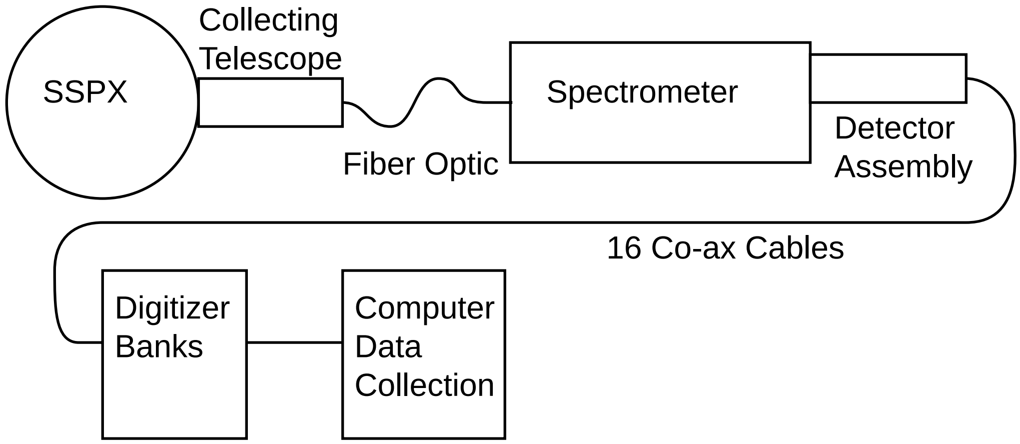

Figure 15: A schematic of the entire IDS system

5.2).

The fiber bundle used to carry the light from the collection telescope to the spectrometer is a custom built cable from Mitsubishi Cable Industries. It is composed of 24 individual 0.25 mm silica fibers, in a circular arrangement (with a diameter of about 1.25 mm) at the collection end, going to a linear arrangement at the output end, with the fibers in a single row of length 6 mm. The linear end of the fiber is butted up against the input slit of the spectrometer and lined up carefully with the direction of the slit to maximize throughput.

The collected light then passes through the spectrometer and comes out at the detector box. The detector assembly is built around a Hamamatsu 16 channel photomultiplier tube (PMT), which consists of 16 0.8 mm $\times$ 16 mm PMTs in a linear array. The tube is mounted in a light-tight box at the output of the spectrometer, with a cylindrical lens magnifying the spectrum and projecting it onto the PMT. Both the PMT and the lens are independently mounted on a rail assembly, so that they can be moved back and forth to adjust the magnification of the detector box. In addition, the lens platform is mounted on a micrometer controlled translation stage, with a shaft to the outside of the box allowing focus adjustment while the box is sealed and the PMT is powered. The final dispersion at the PMT, after magnification, is 0.28 Å/mm.

The output from each of the 16 channels of the PMT is amplified by 16 separate amplifiers with a gain of 1x to 200x, the level of which is controlled remotely by the SSPX operations and data acquisition computers. The signal is then passed to 16 CAMAC digitizers, which record 8 ms of data at a 1 MHz sampling rate beginning at 2 ms before the voltage is applied to the electrodes of the gun in the chamber. This data is then downloaded to a Unix system where analysis can be performed.

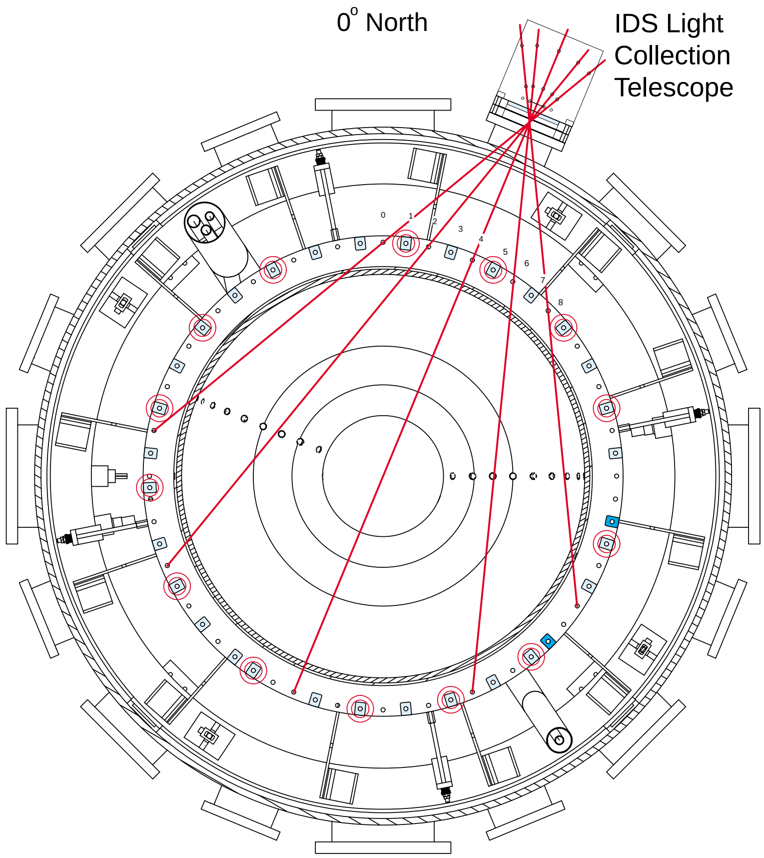

Figure 16: The 5 chords along which the IDS telescope can collect light.

7.2 Design

The most complex design work required for the IDS project was for the detector box. In order to design the assembly, it was necessary to first determine the standard dispersion of the spectrometer, and the dispersion needed to be able to resolve the range of widths that would be seen at the plasma temperatures expected. From equation 42, on page 19, I calculated the linear dispersion of the spectrometer at the output plane to be somewhere around 0.16 nm/mm, using the assumption that θ will be somewhere between $0°$ and $45°$.

It was then necessary to determine the needed dispersion to be able to see Doppler broadening. Table 1 shows the results of using equation 36 to calculate the width in nm of various emission lines at various temperatures. The average width, excluding the H beta lines only included in the table for reference, was around .11 nm. Given that the dispersion is 0.16 nm/mm, this would have only illuminated one channel on the PMT. The solution I used was to magnify the spectrum to increase the dispersion.

From equation 43, on page 20, I used the fact the the grating is about 140 mm wide to calculate a minimum resolvable width through the spectrometer of about 0.002 nm. However, since the input slit is much larger than this, in the 10s of microns range, it is that width that dominates the size of the minimum spectral lines. Thus the minimum resolvable line width is around 0.01 nm, an acceptable value given that line widths at the temperatures of SSPX plasmas an order of magnitude larger than that. I assumed a spectral line of width on the order of 0.1 nm, and decided a good magnification would probably be around 15x, in order to cover the entire PMT array with the spectral line.

In order to determine what type of lens to use to magnify the spectrum, I used the thin lens equation (equation 27, page 14) to examine the magnification achievable using 5 different cylindrical lenses, at varying distances from the focal plane of the spectrometer. Table 2 show the results of these calculations. I decided that the best potential range of magnifications, from between 10x and 20x, was given by the 8mm focal length lens.

7.3 Alignment and Focusing

Aligning the IDS was principally a matter of getting the proper strength signal to the digitizers with the least amount of noise. However, there were a large number of factors that needed to be addressed to ensure a high signal to noise ratio.

The first of these was to make sure that the light collection optic was properly focused onto the fiber optic. This meant making sure that the end of the fiber was at the focal point of the lens. This was checked by illuminating the opposite end of the fiber with a bright white light and looking at the size of the light spot projected by the lens. If the spot had the same diameter as the lens at a large distance from the lens, then the light was being properly collimated. Thus, the light collected by the fiber was only from the narrow column in front of the lens.

The second place where alignment was required was at the input slit. This

DOPPLER WIDTH CALCULATIONS (nm)

	O II	O III	O IV	O V	C II	C III	C V	H beta
wavelength (nm)	441.49	304.71	306.35	278.11	426.7	464.74	227.09	486.13
weight	16	16	16	16	12	12	12	1
Temperature (eV)								
50	0.05993867	0.0413688	0.04159146	0.03775747	0.06689263	0.07285606	0.0356003	0.26399679
100	0.08476608	0.05850432	0.0588192	0.05339712	0.09460046	0.10303402	0.05034642	0.37334784
150	0.10381682	0.07165287	0.07203851	0.06539785	0.11586143	0.12619039	0.06166152	0.45725585
200	0.11987734	0.0827376	0.08318291	0.07551493	0.13378525	0.14571211	0.07120059	0.52799358
250	0.13402694	0.09250345	0.09300132	0.08442826	0.14957646	0.16291109	0.07960468	0.59031477
300	0.14681916	0.10133245	0.10187784	0.09248652	0.1638528	0.17846016	0.08720256	0.64665743
350	0.15858281	0.10945156	0.11004065	0.09989686	0.17698125	0.192759	0.09418953	0.69846985
400	0.16953216	0.11700864	0.1176384	0.10679424	0.18920092	0.20606804	0.10069284	0.74669568
600	0.20763364	0.14330573	0.14407703	0.1307957	0.23172285	0.25238078	0.12332304	0.9145117

Table 1: The table of potential Doppler widths (FWHM, in nm) for various atoms, emission lines, and ion temperatures.

(all in mm)

L1+L2=	175.00	175	175	175	175
f=	4.00	8	10	12.7	19
L2=	170.90	166.60	164.35	161.21	153.31
L1=	4.10	8.40	10.65	13.79	21.69
Magnification=	41.73	19.82	15.44	11.69	7.07
L1+L2=	150.00	150	150	150	150
f=	4.00	8	10	12.7	19
L2=	145.89	141.52	139.23	135.99	127.68
L1=	4.11	8.48	10.77	14.01	22.32
Magnification=	35.47	16.69	12.92	9.71	5.72
L1+L2=	125.00	125	125	125	125
f=	4.00	8	10	12.7	19
L2=	120.86	116.41	114.04	110.65	101.63
L1=	4.14	8.59	10.96	14.35	23.37
Magnification=	29.22	13.55	10.40	7.71	4.35
L1+L2=	100.00	100	100	100	100
f=	4.00	8	10	12.7	19
L2=	95.83	91.23	88.73	85.07	74.49
L1=	4.17	8.77	11.27	14.93	25.51
Magnification=	22.96	10.40	7.87	5.70	2.92
L1+L2=	200.00	200	200	200	200
f=	4.00	8	10	12.7	19
L2=	195.92	191.65	189.44	186.37	178.74
L1=	4.08	8.35	10.56	13.63	21.26
Magnification=	47.98	22.96	17.94	13.67	8.41
lens price	$260.00	$260.00	$260.00	$338.00	$338.00
lens part no (melles griot)	01LQC403	01LQC405	01LQC407	01LQC000	01LQC001

Table 2: Table of magnification possibilities for the detector assembly. Each column is for one specific focal length of cylindrical lens (labeled f in each row), each row is for a specific distance of the detector from the focal point of the spectrometer. L1 is the distance of the lens from the image plane, L2 is the distance of the detector from the lens.

was a fairly difficult task, because of the number of degrees of freedom in the system. The fiber is mounted at the slit on an X-Y translation stage, which allows movement of the end of the fiber across the slit and up and down the length of it. In addition, the angle of the linear end of the fiber is adjustable to get the fiber vertical. The method used to align this system was to set the spectrometer to a strong mercury line and illuminate the input end of the fiber with a mercury light. Care had to be taken so as not to expose the ends of the fiber to the mercury lamp for extended periods of time, as the strong UV component of the light produces ozone from the oxygen in the air which can darken the ends of the fiber and reduce fiber throughput. The detector was powered, and the voltage output of the center channel was monitored on a multimeter. With the slit opened to about 0.5 mm, the angle of the fiber was adjusted to maximize the voltage of the center channel of the detector. The slit was then slowly narrowed to the desired width, and the fiber continuously adjusted using the translation stage to keep the output maximized. It was also necessary to adjust the wavelength setting of the spectrometer to keep the mercury line centered on the detector, as the adjustment of the slit size slightly affected the location of the line.

The output of the spectrometer also needed initial adjustment, and any changes in the magnification of the detector box would require this process again. The second column of table 2 shows the possible magnifications. The 15x magnification was selected by putting the detector 150 mm (l1 + l2 in the table) from the image plane of the spectrometer. The image plane was located approximately by projecting a spectral line on a white piece of paper and noting where the line was sharpest visually. The detector box was then sealed and the detector powered, and a spectral line was lined up with the detector. The focus knob was then adjusted to maximize the peak intensity of the spectral line at the detector, a process which also narrowed the spectral line as much as possible.

7.4 Operation

To operate the IDS, the proper operating voltage must be applied to the PMT. The gain on the PMT is dependent on the input voltage, so one of the main steps in ensuring that the output signal is at an appropriate level is to adjust the input voltage. The theoretical maximum voltage to be used on the PMT is -900 v, so the range of voltages typically used during operations and testing was between -600 v and -800 v. If the signal level at the digitizers was too low, the first thing was to increase the voltage (that is, make it more negative). If the detector saturated during a shot, the voltage was lowered. The gains on the amplifiers were adjusted to put the signal into the level visible by the digitizers, which could only detect voltage changes in increments of 10 mV, but the voltage on the PMT was kept as high as possible without saturation to keep the signal to noise ratio as high as possible.

The PMT needed load resistors between the outputs and ground for proper operation, and the value of these resistors also affected the voltage of the signal. Effectively, the PMT puts out a constant current on each channel proportional to

Resistance	RC time constant
1 kΩ	0.6 μs
10 kΩ	6 μs
220 kΩ	130 μs

Table 3: The relationship between load resistors on the PMT and the RC time constant of the signal line.

light input, and thus the lower the load resistance, the lower the signal voltage. The other condition on the size of the load resistors, however, was that the coaxial signal cable has a small but not insignificant capacitance, about 30 pF per foot. There is about 20 feet of signal cable from the IDS to the equipment racks with the amplifiers and digitizers, so there is a total capacitance of about 600 pF on the line. Thus, the higher the load resistance, the higher the RC time constant of the signal line, which results in a lower time resolution of the system. The decision about what load resistance to use was a decision balancing required signal level and required time resolution, and the load resistance was changed several times in the course of initial operations until a value of 10 kΩ was decided on. This resulted in a RC time constant of $600pF \times 10k\Omega = 6\mu s$. Table 3 shows the various load resistances used and the RC time constant of the signal line for each one. The RC constant for 10 kΩ should be sufficiently small to allow detail of the shots, which last between 1 and 2 ms.

Once all the setup is done and the PMT has power, taking data from a shot is very easy. The entire data acquisition system for SSPX is automated, so the digitizers are automatically triggered at the beginning of a shot, and the data is downloaded the the computer system where data analysis occurs.

8 Ion Temperature Measurements

One of the major difficulties involved in this research was scheduling. Due to SSPX downtime, I was only able to be present during SSPX runs for two days. This caused some difficulty with the working out of the various initial problems with the IDS. However, these were overcome, and some initial IDS data has been acquired. More work will be done with the IDS over the coming summer to get more data, and hopefully to increase the accuracy of the data.

A point that needs clarification about these measurements is the relationship between the temperatures of the impurity ions, which are a minority in the gas, and the majority species of ions, the hydrogen nuclei. While it is possible that the impurity ions and hydrogen ions have different temperatures, [Mayo et al., 1991] showed by directly measuring hydrogen ion temperatures in a spheromak that both the minority and majority species of ions have the same temperatures.

8.1 Data Analysis

Analysis of the collected data from the IDS is performed in the IDL program. An IDL code for analyzing Doppler broadening of spectral lines was written by Karsten J. McCollam, currently at the University of Wisconsin. The analysis assumes that both the line shape of the spectral line and the instrumental response function (the output of the instrument to a very narrow line) are both gaussians. For each data point (one time step) there are 16 channels of data across 4.5 Å. These data are fitted to a gaussian curve using a built in IDL routine. Then, since the dispersion of two convolved gaussians add in quadrature (see appendix C for a proof of this statement), the dispersion of the spectral line is calculated by

$$\sigma_{line} = \sqrt{{\sigma_{out}}^2 - {\sigma_{instrument}}^2} \tag{44}$$

From equation 44, the temperature can be calculated based on equations 35 and 36 in section 5.2. This procedure is repeated for each timestep, giving a time resolved ion temperature measurement of the shot.

8.2 Run Data

Only temperature measurements were obtained in the limited time available to test the IDS instrument. Rotational velocities will be forthcoming as work progresses. However, the limited data collected was sufficient for proof of concept. Actual application of collected data to further understanding of processes in the SSPX machine will have to wait until more time is available for data collection.

Figures 17 and 18 show the processed IDS data with time resolved temperatures, calculated central wavelengths, and selected timesteps of spectral line data from one of the first shots seen with the IDS spectrometer, looking at the OIV line (λ=3063.5 Å). This was also one of the first shots that was fired after

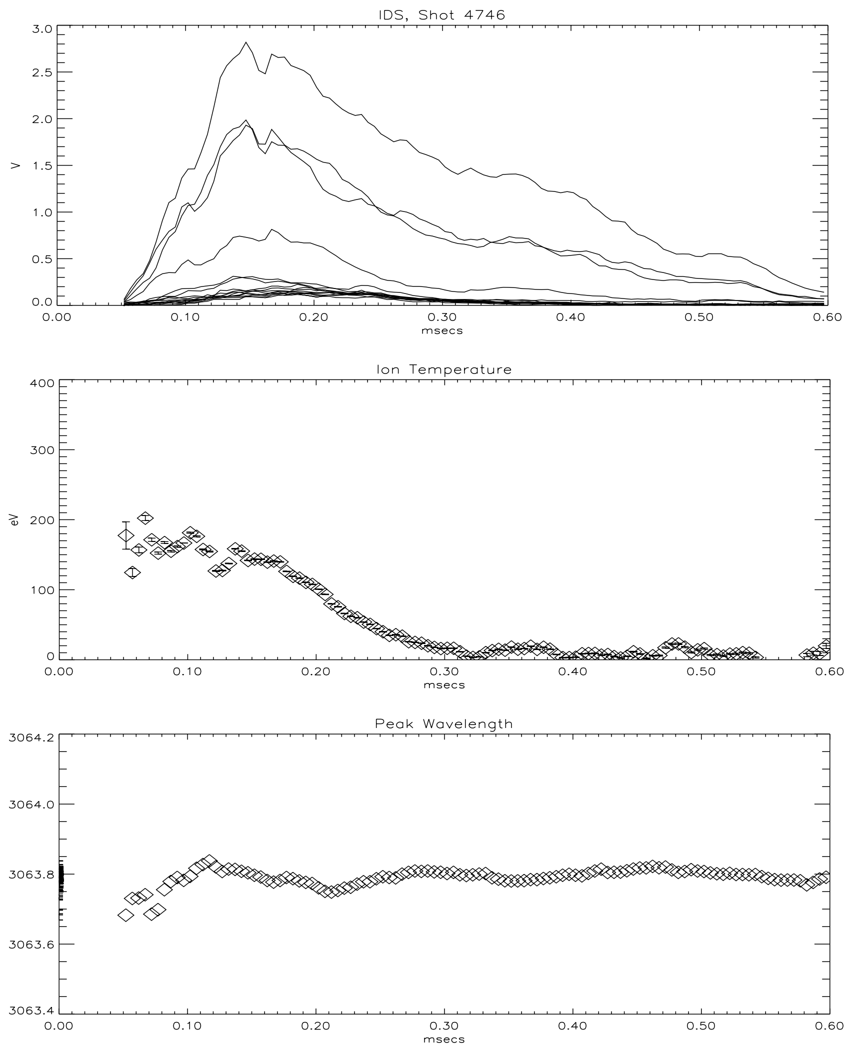

Figure 17: Processed IDS data of the OIV spectral line at 3063.5 Å. The top plot is all 16 IDS channels superimposed. The next plot is the calculated ion temperature as a function of time. The final plot is the calculated center of the spectral line.

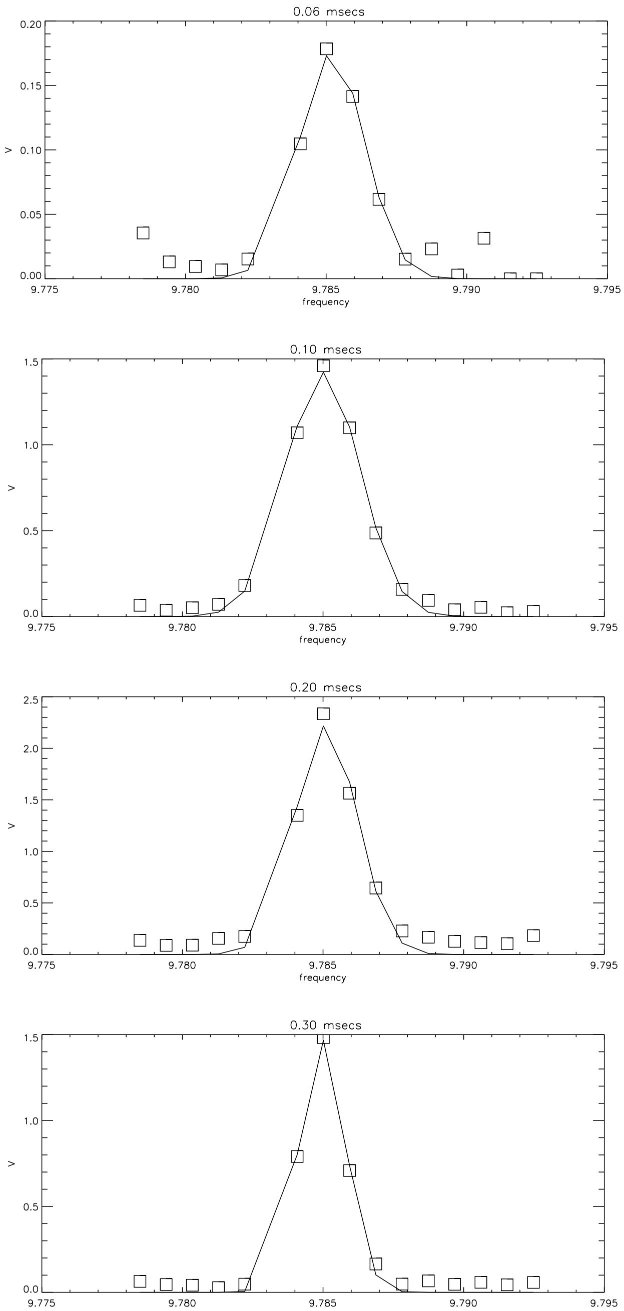

Figure 18: 4 timesteps of the OIV spectral line from the same shot as figure 17. The spectrum visibly narrows at later timesteps as the plasma cools off.

the machine came online after extended downtime, so impurity levels were high and the line was very strong. Peak ion temperatures were around 180 eV, which are on the level of what was expected, given that the peak electron temperatures measured when the machine was very clean and had been functioning well for an extended period of time were at 120 eV. Thus, these measured ion temperatures were definitely hotter than the electron temperatures in the plasma, as expected. The plot of the central wavelength will be used to determine rotational velocities, but further experiments to measure these velocities by changing the view of the light collection telescope have not yet been performed.

Uncertainty in the temperature measurements will also have to wait until further data is acquired. The error bars in figure 17 are based solely on the goodness of fit of the data to a gaussian. These error estimates are quite small, except at the very beginning of the shot when the line intensity is low. However, there is a variance of ± 40 eV in some of the initial timesteps. Further data will be needed to determine whether these fluctuations are real occurrences in the plasma or are artifacts of the data analysis or of other measurement error in the system.

9 Conclusions

The work done for this thesis has led up to a proof of concept that the IDS actually works as expected. No new theoretical understanding has yet been obtained about the SSPX spheromaks, but there is now a measure of ion temperature. However, there is significantly more work to be done with this project.

To begin with, the ion temperature measurements need to be further validated. More data needs to be taken, and similar shots need to be compared to see if the measurements are repeatable, and using this deviation information an error estimate needs to be performed on the temperature data. In addition, data needs to be taken at other emission lines in the spectra, both for oxygen and for other impurities. If the temperature measurements are repeatable over all of these conditions, than they will be further verified.

Once the measurements have been shown to be reliable, the really exciting work can be done with this instrument. The temperature measurements need to be compared with other data, such as magnetic field strength and plasma density measurements, to see if there are correlations. The end goal of this work will be to determine how the ion temperatures in the spheromak plasma are related to reconnection events. This work will continue over the coming summer, as I am returning to LLNL to continue working on the IDS project. With luck, I will be able to use the IDS to achieve some further understanding of the ion heating process.

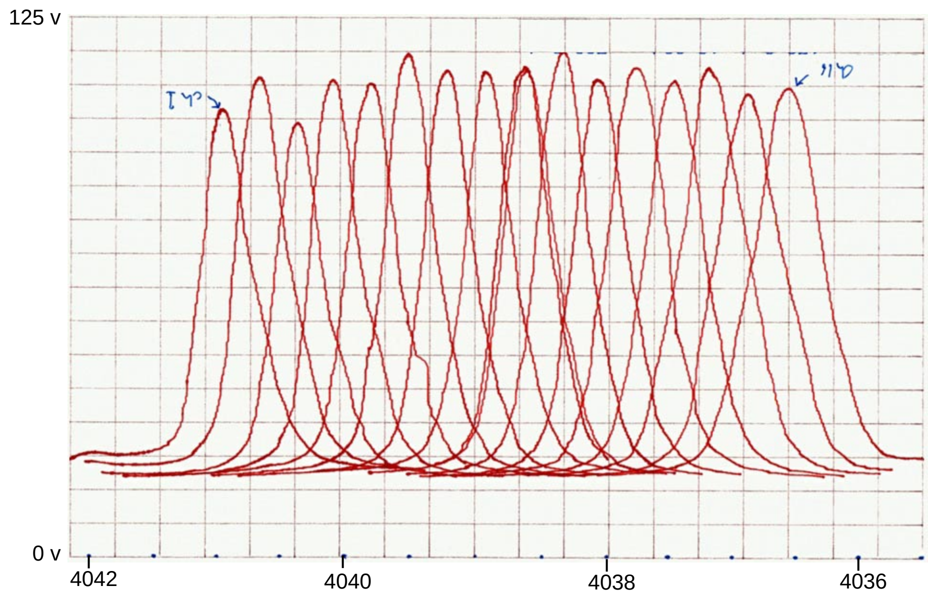

Figure 19: A plot of the response of each channel of the PMT detector to one specific mercury line at 4046 Å. The scale of the y axis is from 0 to 125 mV, and the x axis is in angstroms (Å). There is 0.3 Åbetween channel peaks, and the FWHM of the lines is about 0.55 Å. The slit was set at 0.04 mm.

Appendices

A Spectrometer Calibration - Detector

In order to use a multi channel detector such as the 16 channel PMT used in the IDS detector box, it was necessary to calibrate and normalize each channel's intensity of response to the same signal. To do this, the same mercury line from a calibration lamp was passed over each of the detectors one by one, with the signal output hooked up to an analog plotter. The peak height of each channel was then measured, and a calibration factor was generated for each channel to normalize the output of the detectors. This factor was used as input to the data analysis routine, so that no direct manipulation of the data was required outside of that routine.

B Spectrometer Calibration - Spectral Location

When using any spectrometer, it is usually necessary to find a calibration between the readout of the spectrometer and the actual spectral location. Typically this simply requires using a calibration lamp such as mercury, with a few

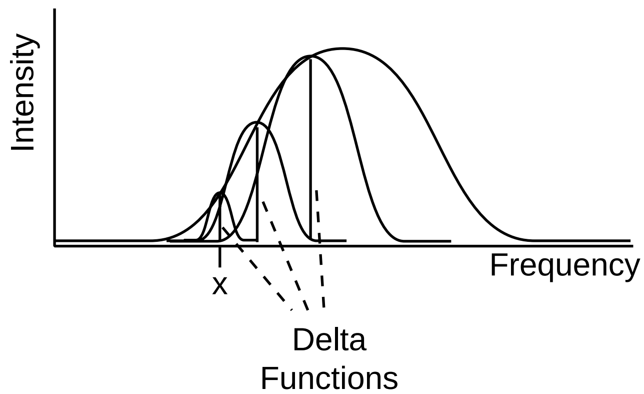

Figure 20: A broad spectral line broken down into delta functions, with the IDS instrumental response to each individual delta function superimposed

very bright lines; each is located with the spectrometer and the relationship is plotted between actual line location and the measured location.

With the THR-100 spectrometer used for the IDS, this process was slightly more difficult due to the age of the instrument, which was approximately 20 years old, and not in perfect mechanical shape. When the initial calibration runs were performed, the location of any individual spectral line, over the course of several calibration runs, was found over a range of about 10 Å. This was enough uncertainty to make locating spectral lines difficult, as the detector only covers a range of 10 Å. In order to repair this, it was necessary to disassemble the entire spectrometer mechanism and re-lubricate it. Following this procedure, the uncertainty in spectral location was reduced to about 0.2 Å.

The dial on the spectrometer was calibrated to a grating with a line density of 1200 lines/mm, so it read about twice as high as the actual line. The final calibration curve for the spectrometer was

$$\lambda = 0.5009d - 5.3 \tag{45}$$

where λ is wavelength in angstroms, and d is the dial reading of the spectrometer. This relation was obtained by locating 4 spectral lines of mercury over a range of 1200 Å, and determining a linear curve fit for the data.

C Convolution of Gaussians

Because the IDS instrument has an instrumental profile, the spectrum at the output is different from the input spectrum. The actual output is a convolution of the input spectra and the instrument profile. To see this, we consider in figure 19 the detected response of the IDS instrument to a very narrow line (a cold mercury line). We can think of this as the response of the instrument to a delta function, since the width of the mercury line is much smaller than the measured line width of 0.55 Å. If we then consider the input signal as being a sum of very close together delta functions, we can see that the total system response to the input signal will be the sum of responses to each of the delta functions (see figure 20). If the intensity of the delta function at a specific wavelength λ is given by $Int(\lambda)$, and the instrumental response is given by $R(d)$, where d is the displacement from the center of the symmetric response function, then the intensity at a specific $\lambda = x$ at the output can be represented as the sum

$$I(x) = \cdots + Int(x) \cdot R(0) + Int(x+\delta) \cdot R(\delta) + Int(x+2\delta) \cdot R(2\delta) + \cdots \tag{46}$$

where δ is the infintesmal displacement to the next delta function. In the limit as δ becomes very small, is is clear that

$$I(x) = \int_{-\infty}^{\infty} Int(x+\delta) \cdot R(-\delta) d\delta \tag{47}$$

This is a standard convolution integral.

If both the input spectrum and the instrumental response are gaussians (or can be approximated as gaussians), this convolution integral which represents intensity at the output of the spectrometer has nice properties which can be exploited to make the data analysis for finding ion temperatures easier. We will assume that the intensity of the incoming spectrum is given by

$$Int(\lambda) = C \cdot exp\left[-\frac{1}{2}\left(\frac{\lambda - \lambda_0}{\sigma_i}\right)^2\right] \tag{48}$$

and the instrumental response has the form

$$R(\delta) = C \cdot exp\left[-\frac{1}{2}\left(\frac{\delta}{\sigma_r}\right)^2\right] \tag{49}$$

We will ignore constants in the following derivation and include them all in C, a constant whose definition will change throughout the calculation.

From equation 47, with a change of variable $\lambda = \lambda - \lambda_0$, we can see that the output intensity is given by

$$\begin{aligned} I(\lambda) &= C\int_{-\infty}^{\infty} exp\left[-\frac{1}{2}\left(\frac{\lambda+\delta}{\sigma_i}\right)^2\right] exp\left[-\frac{1}{2}\left(\frac{-\delta}{\sigma_r}\right)^2\right] \\ &= C\int_{-\infty}^{\infty} exp\left[-\frac{1}{2}\left(\frac{\delta^2({\sigma_r}^2+{\sigma_i}^2) + 2\lambda\delta{\sigma_r}^2 + \lambda^2{\sigma_r}^2}{{\sigma_r}^2{\sigma_i}^2}\right)\right] d\delta \end{aligned} \tag{50}$$

At this point, we complete the square in the exponent, giving

$$I(\lambda) = C\int_{-\infty}^{\infty} exp\left[-\frac{1}{2}\left(\frac{\left(\frac{{\sigma_r}^2+{\sigma_i}^2}{\sigma_r\sigma_i}\delta + \frac{\lambda\sigma_r}{\sigma_i}\right)^2 + \lambda^2}{{\sigma_r}^2+{\sigma_i}^2}\right)\right] d\delta \tag{51}$$

Making the substitution

$$u = \frac{{\sigma_r}^2 + {\sigma_i}^2}{\sigma_r \sigma_i}\delta + \frac{\lambda \sigma_r}{\sigma_i}, \quad du = \frac{{\sigma_r}^2 + {\sigma_i}^2}{\sigma_r \sigma_i} \tag{52}$$

again dropping constants, gives

$$I(\lambda) = C \int_{-\infty}^{\infty} exp\left[-\frac{1}{2}\left(\frac{u^2 + \lambda^2}{{\sigma_r}^2 + {\sigma_i}^2}\right)\right] du \tag{53}$$

Finally, since the integral of a gaussian over all space is a constant, we can pull out the λ dependence from the integral, leaving just a constant behind. Replacing λ with $\lambda - \lambda_0$ as our original variable, we have an instrumental output intensity of

$$I(\lambda) = C \cdot exp\left[-\frac{1}{2}\left(\frac{(\lambda - \lambda_0)^2}{{\sigma_r}^2 + {\sigma_i}^2}\right)\right] \tag{54}$$

Thus, we see that when two gaussians are convolved, their σ's add in quadrature. This enormously simplifies deconvolution. If the output spectrum from a spectrometer is a gaussian, and the instrumental function is also a gaussian, than the σ of the incoming gaussian line profile is simply

$$\sigma_{in} = \sqrt{{\sigma_{out}}^2 - {\sigma_r}^2} \tag{55}$$

Acknowledgements

I would like to thank Dave Hill, Bick Hooper, Harry McLean, and the rest of the SSPX team at LLNL for their help and support on the IDS project. I would like to thank my thesis advisor, Michael Brown, for his help with preparing this thesis, and the entire physics and astronomy department at Swarthmore College for their guidance on this project and over the past 4 years. Finally, I would like to thank my family for all the encouragement and support they have given me; without them, this would have been impossible.

References

[Bellan, 2000] Bellan, P. M. (2000). *Spheromaks: A Practical Application of Magnetohydrodynamic Dynamos and Plasma Self-Organization*. Imperial College Press, London.

[Chen, 1984] Chen, F. F. (1984). *Introduction to Plasma Physics and Controlled Fusion*. Plenum Press, New York.

[Fernández et al., 1990] Fernández, J. C., Jarboe, T. R., Knox, S. O., Henins, I., and Marklin, G. J. (1990). Ion heating and current drive from relaxation in decaying spheromaks in mesh flux conservers. *Nuclear Fusion*, 30:67.

[Geddes, 1997] Geddes, C. G. R. (1997). Equilibrium studies on ssx. Undergraduate thesis, Swarthmore College.

[Geddes et al., 1998] Geddes, C. G. R., Kornack, T. W., and Brown, M. R. (1998). Scaling studies of spheromak formation and equilibrium. *Physics of Plasmas*, 5:1027.

[Gibson et al., 1995] Gibson, K. J., Gee, S. J., and Rusbridge, M. G. (1995). Ion energy measurements in the sphex spheromak. *Plasma Physics and Controlled Fusion*, 37(1):31.

[Hartog and Holly, 1997] Hartog, D. J. D. and Holly, D. J. (1997). A simple, low-cost, versatile charge-coupled device spectrometer for plasma spectroscopy. *Review of Scientific Instruments*, 68(1):1036.

[Hill et al., 2000a] Hill, D. N. et al. (2000a). Overview of spheromak experiments on sspx. APS 2000 Poster Session.

[Hill et al., 2000b] Hill, D. N. et al. (2000b). Spheromak formation studies in sspx. In *18th International Atomic Energy Agency Fusion Energy Conference*. IAEA.

[Hollas, 1996] Hollas, J. M. (1996). *Modern Spectroscopy*. John Wiley and Sons, New York, 3 edition.

[Hooper, 1996] Hooper, E. B. (1996). Introduction to the spheromak. Personal Communication.

[Hooper et al., 1998] Hooper, E. B. et al. (1998). The spheromak path to fusion. Lawrence Livermore National Laboratory Report UCRL-ID-130429.

[Hooper et al., 1999] Hooper, E. B., Pearlstein, L. D., and Bulmer, R. H. (1999). Mhd equilibria in a spheromak sustained by coaxial helicity injection. *Nuclear Fusion*, 39:863.

[Hsu et al., 2000] Hsu, S. C., Fiksel, G., Carter, T. A., Ji, H., Kulsrud, R. M., and Yamada, M. (2000). Local measurement of nonclassical ion heating durring magnetic reconnection. *Physical Review Letters*, 84(17):3859.

[Hutchinson, 1987] Hutchinson, I. H. (1987). *Principles of Plasma Diagnostics.* Cambridge University Press, Cambridge.

[Jenkins and White, 1976] Jenkins, F. A. and White, H. E. (1976). *Fundamentals of Optics, 4th ed.* McGraw-Hill, New York.

[Kornack, 1998] Kornack, T. W. (1998). Magnetic reconnection studies on ssx. Undergraduate thesis, Swarthmore College.

[Krall and Trivelpiece, 1973] Krall, N. A. and Trivelpiece, A. W. (1973). *Principles of Plasma Physics.* McGraw-Hill, New York.

[Lukin, 2000] Lukin, V. (2000). Modeling ssx spheromak plasmas: internal physics from external measurements. Undergraduate thesis, Swarthmore College.

[Mayo et al., 1991] Mayo, R. M., Fernández, J. C., Henins, I., Kirschenbaum, L. S., Munson, C. P., and Wysocki, F. J. (1991). Time of flight measurements of ion temperatures in spheromaks. *Nuclear Fusion*, 31:2087.

[Mayo et al., 1993] Mayo, R. M., Hurlburt, D. J., and Fernández, J. C. (1993). Ion temperature profile deconvolution and corrections to confinement parameters in spheromaks. *Physics of Fluids B*, 5(11):4002.

[McLean et al., 2001] McLean, H. S. et al. (2001). Plasma diagnostics for the sustained spheromak physics experiment. *Review of Scientific Instruments*, 72(1):556.

[Ono et al., 1996] Ono, Y., Yamada, M., Akao, T., Tajima, T., and Matsumoto, R. (1996). Ion acceleration and direct ion heating in three-componant magnetic reconnection. *Physical Review Letters*, 76:3328.

[Reif, 1965] Reif, F. (1965). *Fundamental os Statistical and Thermal Physics.* McGraw-Hill, New York.

[Taylor, 1974] Taylor, J. B. (1974). Relaxation of toroidal plasma and generation of reverse magnetic fields. *Physical Review Letters*, 33:1139.